RE-565

METALLURGICAL ANALYSIS OF SKYLAB M552 AND M557 SAMPLES

December 1978

RESEARCH DEPARTMENT

GRUMMAN AEROSPACE CORPORATION
BETHPAGE NEW YORK

Grumman Research Department Report RE-565

METALLURGICAL ANALYSIS OF SKYLAB M552 AND M557 SAMPLES

Final Report - Prepared for

George C. Marshall Space Flight Center
National Aeronautics and Space Administration
Marshall Space Flight Center, Alabama 35812

by

D. J. Larson, Jr.
Research Department
Grumman Aerospace Corporation
Bethpage, New York 11714

This investigation was partially funded by the
National Aeronautics and Space Administration
under Contract NAS8-28728

December 1978

Approved by: Richard A. Scheuing
Richard A. Scheuing
Director of Research

ABSTRACT

Previous reports have noted anomalous microstructures and unknown diffraction spectra for the Skylab M557 and M552 flight samples. This work explains the anomalous microstructures on the basis of phase equilibria, liquid/liquid phase separation, and liquid/solid segregation. All of the unknown diffraction spectra have been identified. The previously unknown crystal structure of the Zn_3Sb_2 phase in the M557B Experiment has been determined. Previously unreported effects due to the near-absence of the hydrostatic pressure head are documented for the M557C samples.

TABLE OF CONTENTS

PAGE IV INTENTIONALLY BLANK

LIST OF ILLUSTRATIONS

LIST OF TABLES

INTRODUCTION

This program was undertaken to identify the origin of the anomalous diffraction spectra and microstructures reported for the Skylab M557 and M552 flight samples.

The Skylab M557 experiment processed three alloys that demonstrated appreciable macrochemical segregation as the result of terrestrial processing. These alloys were a hypereutectic Au-Ge alloy, a ternary Pb-Zn-Sb hypermonotectic alloy, and a ternary eutectic Pb-Sn-In alloy. The last was directionally solidified using a Bridgman technique. The objective of the experiment was to determine the significance of virtually eliminating the gravitationally driven segregation mechanisms on the phase equilibria, morphology, microstructure, and electromagnetic performance (superconductivity and resistivity) of the samples. The Au-Ge and Pb-Zn-Sb flight samples were reported to exhibit unknown diffraction spectra and a more uniform value of resistivity over the length of the samples. In addition, a superconducting transition, of unknown origin, was found in the Pb-Zn-Sb flight samples.

The Skylab M552 experiments demonstrated the engineering feasibility of using brazing as a repair technique in orbit. A commercial Cu-Ag-Li brazement with stainless steel or nickel as base metal was used. Anomalous microstructures were noted within the flight samples.

This report describes the samples that demonstrated liquid/liquid immiscibility (M557B and M552) and then reports on those that demonstrated liquid/solid limited miscibility (M557A and M557C).

EXPERIMENTAL RESULTS AND DISCUSSION

LIQUID/LIQUID IMMISCIBILITY

The Skylab experiments that addressed, or encountered, liquid/liquid immiscibility were M557B, M552, and a science demonstration experiment. The M557B and M552 experiments are described in detail.

M557B Ternary Immiscibility

The M557B experiment conducted by Reger (Ref. 1-4) processed a liquid/liquid immiscible ternary alloy consisting of 45.05% Pb, 45.06% Zn, and 9.89% Sb by weight. It was anticipated that the low-g environment would minimize the rate of settling due to gravitationally driven Stokes migration and would thus result in a uniformly dispersed solidification product. It was thought that the low-g environment would also minimize the coalescence due to gravitationally driven thermal or solutal convection and Stokes migration, and that the particle size distribution within the orbitally processed samples would thus be considerably finer than in the terrestrially processed samples. Although the particle dispersion within the flight samples was more uniform, the particle size was found to be macroscopic in dimensions, which was unanticipated.

In addition to particle size and distribution differences, unknown x-ray diffraction spectra and an additional superconducting transition were reported for the flight samples. This naturally led to the consideration that the orbital environment was in some unexpected fashion promoting metastability.

The objective of our analysis of the six ground-base and three flight samples was to determine the origin of the anomalous x-ray and superconducting data and to determine whether there were gravitationally dependent modifications of the phase equilibria.

Our study began with a determination of the terrestrial binary and ternary phase equilibria. On the basis of thermal analysis data, Klodt (Ref. 5) has reported that this alloy has a consolute temperature of 877K (604°C) and ternary reaction isotherms at 706K (433°C), 671K (398°C), 620K (347°C), and 580K (307°C). The binary phase diagrams and

the ternary phase diagram at, or slightly above, 706K (433°C) are shown in Fig. 1. The time in the region between the consolute temperature 873K (604°C) and the initial ternary reaction isotherm, 706K (433°C), is a function of the cooling rate through this region. The reaction that Klodt (Ref. 5) reports at 706K (433°C) marks the formation of a ternary liquid phase, L_3, that can coexist with both the L_1 and L_2 phases. The formation of the liquid, L_3, via a ternary peritectic-class reaction occurs at L_1/L_2 interfaces and serves to lessen the total interfacial free energy of the system. Microchemical analyses of the regions that we have identified as solidified liquid L_3 indicate that it is approximately 60 atomic % Zn and 40 atomic % Sb, with a trace of Pb. The morphology of these regions indicates that this was not the first region to solidify.

The reaction at 671K (398°C) marks the solidification of the primary monotectic phase, L_2. The microstructure resulting from the solidification of this Zn-rich liquid is shown in Fig. 2. This microstructure appears to be primary Zn (β) with secondary eutectic, consisting of Zn (β) + Zn_3Sb_2(η), filling in the last regions to solidify.

The reaction at 620K (347°C) marks the solidification of the ternary liquid phase, L_3, that formed at 706K (433°C). This phase served to separate the Zn-rich and Pb-rich regions. The effectiveness with which it did so is shown in Fig. 3. The microchemical distribution of Zn, Sb, and Pb within the region shown in Fig. 3 are shown in Figs. 4, 5, and 6.

The reaction at 580K (307°C) marks the solidification of the secondary monotectic liquid, L_1. The solidification product of this Pb-rich liquid is shown in Fig. 7. The microstructure consists of a few elongated primary Zn_3Sb_2(η) particles (the area shown is atypical) with Zn particles in a Pb matrix. Energy dispersive analyses of the Pb-rich regions indicate that the central core of the Pb-rich regions is somewhat poorer in Zn than the outer regions.

Primary crystallization of Zn_3Sb_2(η) occurred locally in both the Zn-rich, L_2, and Pb-rich, L_1, liquids. These crystals appeared monolithic and seemed to reflect crystal symmetries that were dependent on the temperature of solidification. The Zn_3Sb_2(η) primary crystallites within the Zn-rich, L_2, region solidified at temperatures in excess of 671K (398°C).

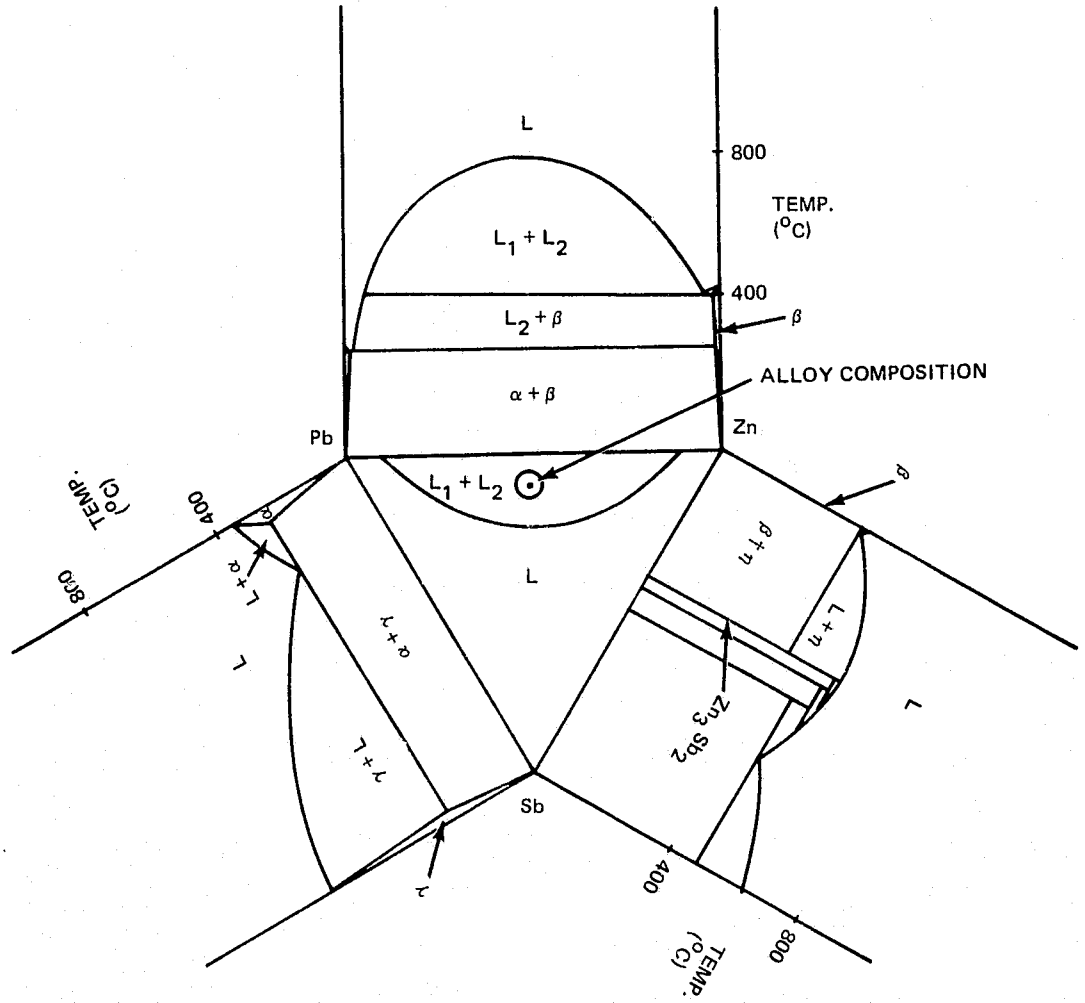

Fig. 1 Binary Phase Diagrams for Pb-Zn-Sb and Ternary Isothermal Section Taken Slightly Above 706K (433°C)

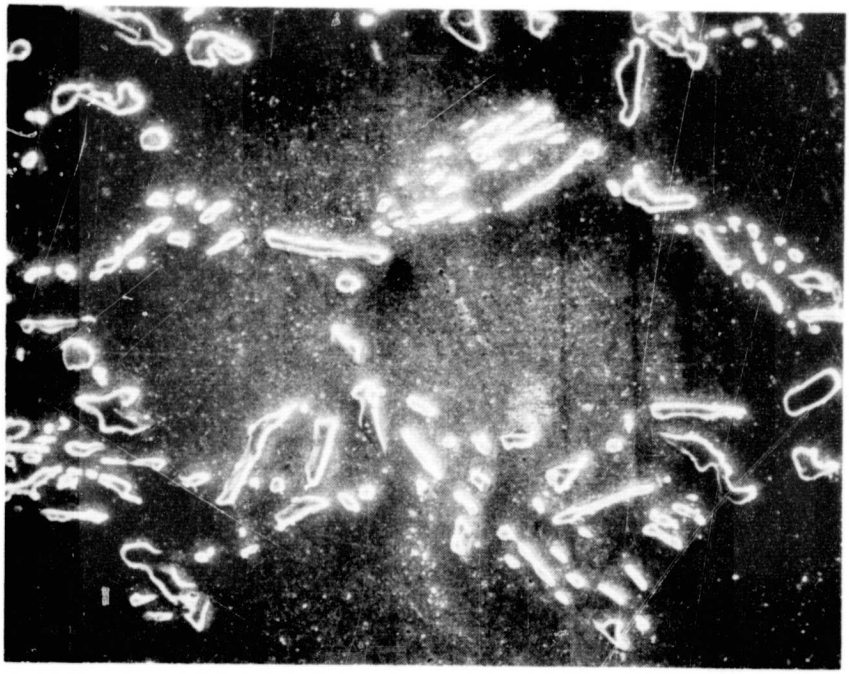

Fig. 2 Solidification Structure of the Primary Monotectic Liquid, L_2, Consisting of Pro-Eutectic Zn (β) Grains with Eutectic Zn (β) + Zn_3Sb_2 (η) at the Grain Boundaries (1000 X)

Fig. 3 Photomicrograph Showing the Solidified L_3 Region (Medium Gray) Acting as a Barrier to Contact Between the Solidified Zn-Rich, L_2, (Dark Gray) and Pb-Rich, L_1, (Light Gray) Regions (200 X)

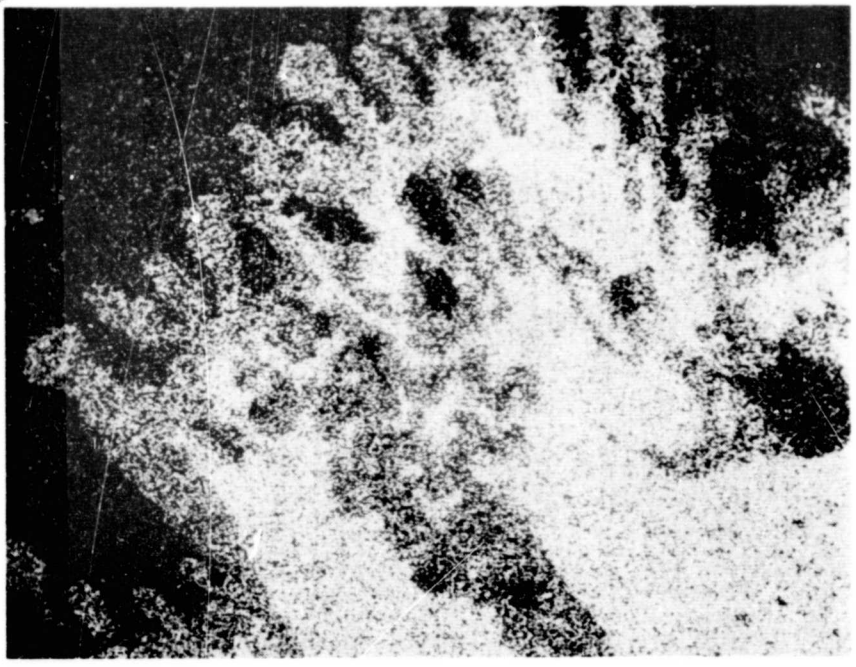

Fig. 4 Zinc Distribution in the Region Shown in Fig. 3 (200 X)

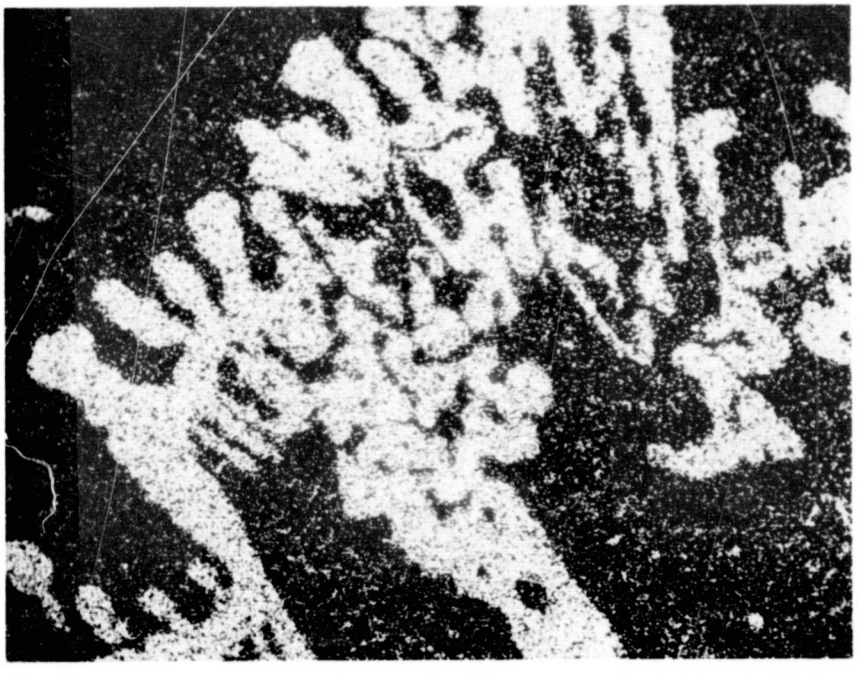

Fig. 5 Antimony Distribution in the Region Shown in Fig. 3 (200 X)

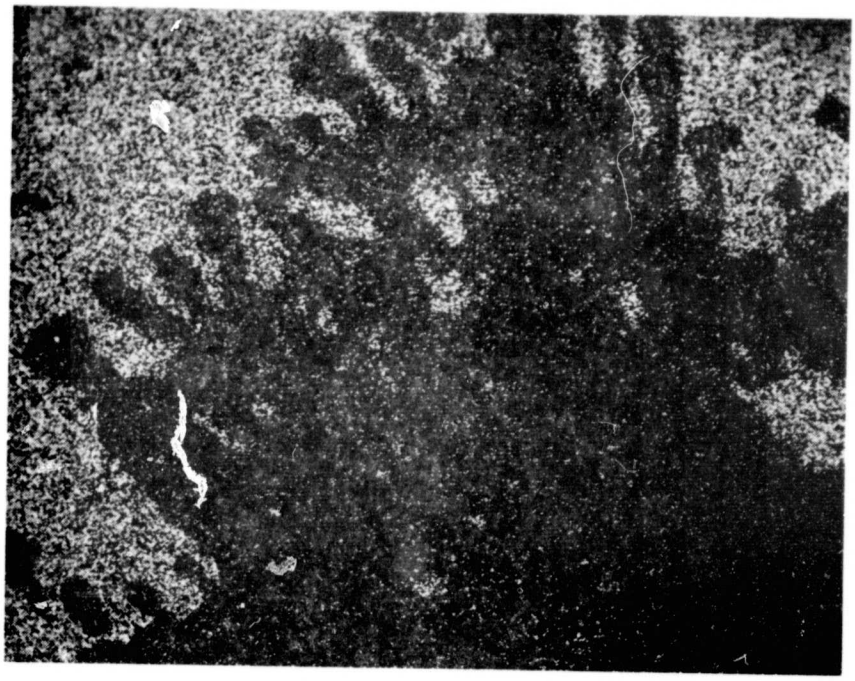

Fig. 6 Lead Distribution in the Region Shown in Fig. 3 (200 X)

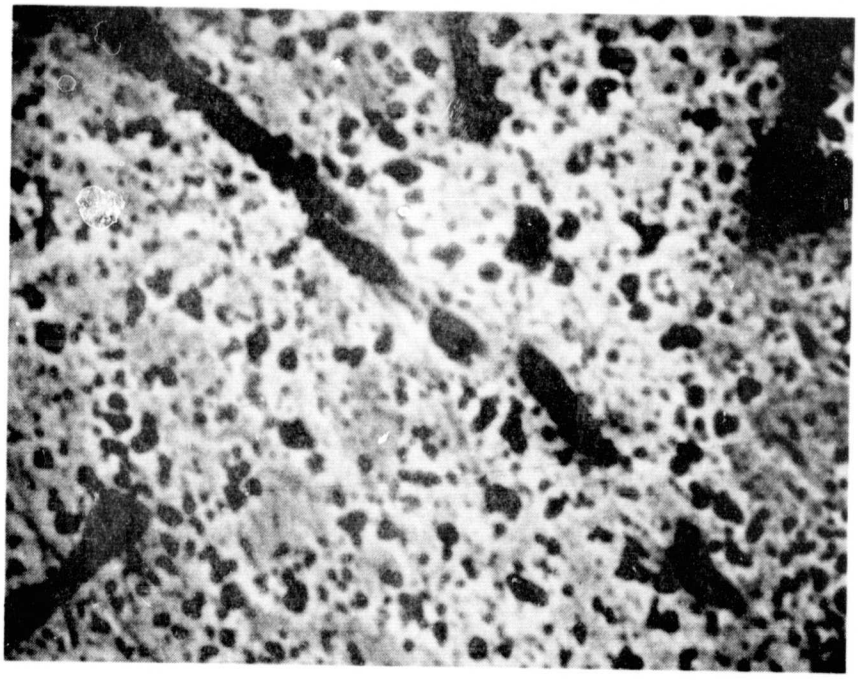

Fig. 7 Solidified Structure of the Secondary Monotectic Pb-Rich Liquid, L_1 (5000 X)

The crystal symmetry is shown in Fig. 8. It appears that the crystal structure is hexagonal with solidification occurring on the prismatic planes in the 'c' direction. This results in a core of solidified liquid that has been entrapped by the closure of the prismatic planes. This is shown in Fig. 8, where the growth direction is normal to the plane of the figure.

The $Zn_3Sb_2(\eta)$ primary crystallites that were found in the Pb-rich, L_1, regions were also monolithic, but appeared to have a different growth system. Solidification was no longer on the prismatic planes, although these particles appear hexagonal. This is shown in Fig. 9. The hexagonal structure in Fig. 9 could be a truncated section of a lower symmetry crystal structure. Microchemical analysis of precipitates within the Zn-rich and Pb-rich liquids could not distinguish between them.

We have also characterized the microstructures of the ground base samples and found that the distribution of the microstructures was quite different in the ground base samples than in the flight samples. The ground base samples consisted of a top-most Zn-rich layer, solidifed L_2, a bottom-most Pb-rich layer, solidified L_1, and a Zn_3Sb_2-rich region, solidified L_3, separating the two. The flight samples had a more uniform distribution of the three regions.

Reger (Refs. 1 and 2) reported unknown x-ray diffraction lines within the diffraction spectra of the flight samples. The unknown diffraction lines are shown in Table 1, column 1. Reger did not publish a tabulation of his complete spectra. He suggests, however, that some of the unknown diffraction lines are due to higher order reflections of the constituent elements. We have examined this possibility. Calculated diffraction spectra for the Pb and Zn phases are presented in Table 1, columns 2 and 3. Pb was considered to be face centered cubic (FCC) with a lattice parameter, a_o, of 4.950 Å; Zn was taken to be hexagonal close packed (HCP) with lattice parameters of 2.664 Å and 4.945 Å in the a_o and c_o directions, respectively. The crystal structure of the $Zn_3Sb_2(\eta)$ phase is unknown. It is clear that some of the diffraction lines that Reger (Refs. 1 and 2) reported as unknowns are attributable to Pb and Zn reflections.

Our diffraction spectra are presented in Table 2, with the identification of each diffraction line indicated, where known. We suspected that the

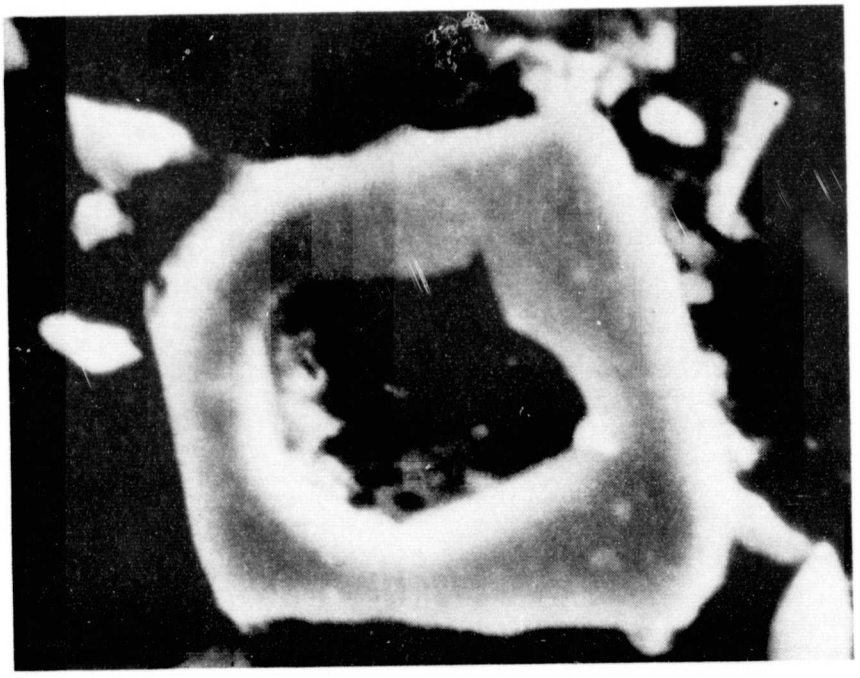

Fig. 8 Prismatic Solidification Morphology of the Primary Zn_3Sb_2 Phase That Precipitated from the Zn-Rich Liquid, L_2 (5000 X)

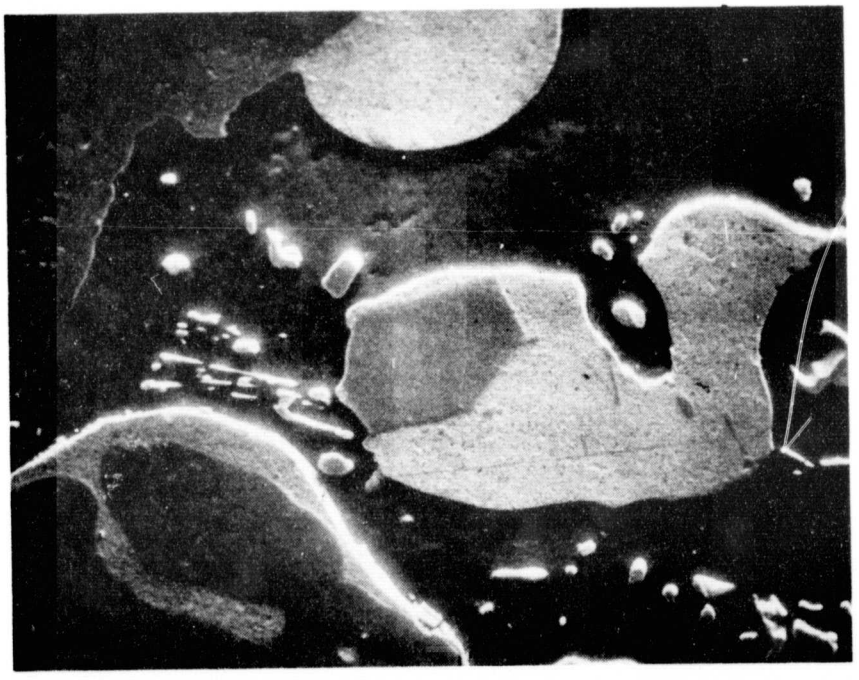

Fig. 9 Primary Zn_3Sb_2 Particle (Central Hexagon) that Precipitated from the Pb-Rich Liquid, L_1 (500 X)

TABLE 1 REPORTED AND CALCULATED X-RAY DIFFRACTION SPECTRA FOR M557B SAMPLES

Unknown Diffraction Lines (1,2)	Calculated Diffraction Spectra				
	Pb(α)		Zn(β)		Zn_3Sb_2(η)
d	d	{hkl}	d	{hkl}	
3.450			4.945	{001}	Unknown
3.437	2.858	{111}			
2.976	2.475	{200}			
2.673			2.473	{002}	
2.657			2.307	{100}	
2.313			2.091	{101}	
2.135	1.750	{220}			
2.043			1.687	{102}	
2.039			1.648	{003}	
2.036	1.492	{311}			
2.004	1.429	{222}			
1.489			1.341	{103}	
1.336			1.332	{110}	
1.310	1.237	{400}	1.236	{004}	
1.295			1.156	{200}	
1.255	1.136	{331}			
1.186			1.123	{201}	
1.133	1.107	{420}			
1.113			1.045	{202}	
1.008*	1.010	{422}			

*For experimental reasons we terminated our experiments at d = 1.000 Å. Our comparisons are limited to this regime.

TABLE 2 EMPIRICAL DIFFRACTION SPECTRA FOR GROUND BASE AND SKYLAB FLIGHT M557B SAMPLES

d Spacings		Origin
Ground Base	Flight	Phase, Reflecting Plane
	4.419	Zn_3Sb_2 {004}
3.525	3.520	Zn_3Sb_2 {005} {200}
3.422	3.414	Zn_3Sb_2 {201}
3.361	3.358	Zn_3Sb_2 {113}
	3.150	Zn_3Sb_2 {105}
3.104	3.100	Sb {102}
2.975	2.981	Zn_3Sb_2 {114}
2.851	2.849	Pb {111}
	2.801	Sb {004}
	2.731	Zn_3Sb_2 {204}
	2.691	Zn_3Sb_2 {106}
	2.650	Zn_3Sb_2 {115}
2.472	2.462	Pb, {200} ; Zn, {002}
2.307	2.301	Sn {100}
	2.265	Zn_3Sb_2 {214} Sb {014}
	2.229	Zn_3Sb_2 {206}
2.131	2.129	Zn_3Sb_2 {215}
2.089	2.084	Zn {101}
2.037	2.033	Zn_3Sb_2 {220}
2.016	2.014	Zn_3Sb_2 {221}
	2.000	Zn_3Sb_2 {216}
1.958	1.958	Zn_3Sb_2 {310}{009}{305}
	1.932	Zn_3Sb_2 {311}
1.912		Zn_3Sb_2 {312}
1.895		Zn_3Sb_2 {208}
1.748	1.747	Pb {220}
1.715	1.713	Zn_3Sb_2 {315}
1.689	1.684	Zn {102}
	1.622	Zn {003}
1.491	1.490	Pb {311}

TABLE 2 EMPIRICAL DIFFRACTION SPECTRA FOR GROUND BASE AND SKYLAB FLIGHT M557B SAMPLES (Cont'd)

d Spacings		Origin
Ground Base	Flight	Phase, Reflecting Plane
1.4731		Zn_3Sb_2 {0012}
	1.433	Zn_3Sb_2 {326}
1.4277	1.427	Pb {222}
	1.418	Zn_3Sb_2 {500}
	1.340	Zn {103}
	1.331	Zn {110}Zn_3Sb_2 {330}
1.2425	1.242	Zn_3Sb_2 {425}
	1.236	Zn_3Sb_2 {513}
	1.172	Zn_3Sb_2 {600}{0015}
	1.153	Zn {200}
1.1350	1.135	Pb {331}Zn_3Sb_2 {604}
1.1230	1.124	Zn {201}
1.1063	1.106	Pb {420}
	1.089	Zn_3Sb_2 {606}
	1.070	Zn_3Sb_2 {610}
	1.010	Pb {422}

majority of the unknown diffraction lines were due to the $Zn_3Sb_2(\eta)$ phase. As a consequence we analyzed sections of the ground base samples that maximized this constituent. Considering that the parent elements (Zn and Sb) are hexagonal, that one of the structural modifications of the adjacent Zn_4Sb_3 phase is complex hexagonal, and that the solidification morphology of the Zn_3Sb_2 phase indicates that the structure is hexagonal, we imposed a hexagonal solution on the unknown lines of the diffraction spectra. This has been successful, and a complex hexagonal unit cell with a_o and c_o parameters of, respectively, 8.139 and 17.677 Å is proposed. This structure can account for all of the unknown diffraction lines except those at 3.100 and 2.801 Å, and it is proposed that these lines are attributable to small quantities of Sb, which precipitates from the Pb-rich liquid or saturated solid solution. Because of the extremely low intensities involved, it was not possible to compare calculated intensities with those measured in order to infer the specific locations of the Sb and Zn atoms in the Zn_3Sb_2 structure. It is sufficient to confirm that a complex hexagonal $Zn_3Sb_2(\eta)$ structure of the above dimensions can account for all of the heretofore unknown diffraction lines.

It would then appear that the more homogeneous distribution of the Zn_3Sb_2 phase in the flight samples has resulted in its presence being noted in the x-ray diffraction spectra of these samples. Another possibility is that an increased L_1/L_2 interfacial area within the flight samples offered the opportunity for the reaction forming the tertiary liquid, L_3, to go further to completion. Solidification of increased percentages of L_3 would result in increased amounts of Zn_3Sb_2. In any case, the origin of the unknown diffraction lines is the Zn_3Sb_2 phase and not an anomalous metastable phase.

M552 Exothermic Brazing

The M552 Skylab Experiment investigated the feasibility of using brazing as a repair or fabrication process in space. An exothermic reaction was utilized as a heat source for a commercially available eutectic brazement of 71.7 Ag-28.0 Cu - 0.3 Li (wt.%). Four tubing/sleeve simulated structures were brazed. The base metals used for the tubing and sleeve were either commercially pure nickel or 304L stainless steel.

Two of each type were brazed. The brazement rings were housed in a machined circumferential groove on the inner diameter of the sleeve and acted as a reservoir of brazement material. Flow from this starting point could be measured. The gap widths were varied in order to test stability criteria for liquid columns in low-g.

The flight samples were found to exhibit more uniform menisci, increased liquid spreading, and reduced porosity. Specimens with a wide gap geometry were successfully processed, whereas these fluid configurations are geometrically unstable in the earth's gravitational environment.

The ground base samples exhibited normal eutectic microstructures for both the nickel base metal and stainless steel base metal cases. This is shown in Fig. 10. The ground base and flight samples are denoted by an MC or SL sample code, respectively. Nickel and stainless steel base metal samples are indicated by placement of an N or an S, respectively, after the previous sample code (e.g. MCN or MCS). The flight samples, however, all exhibited anomalous microstructures. These are shown in Figs. 11a and 11b. Our work was undertaken to determine the origin of these anomalous microstructures.

In order to explain the anomalous microstructures within the flight samples, we first looked at the phase relationships. The first phase relations to consider are those of the braze alloy. The Cu-Li and Ag-Li binary phase diagrams are shown in Figs. 12a and 12b, respectively. It is clear that lithium is virtually immiscible in copper, and that almost all of the lithium would be anticipated to be in the silver terminal solid solution phase. If all of it were tied up in the silver phase, it would be expected to suppress the silver phase solidus temperature to about 1150K (880°C). The ternary Ag-Cu-Li eutectic might also be nominally affected. However, we would expect no dramatic impact in phase relations to result from this low level ternary addition, and the microstructures support this contention.

We hypothesized that the phase separation within the SLS-3 flight sample was the result of liquid/liquid immiscibility. As a result, the first thing that we considered was the relative stability of the Ag-Cu-Li eutectic liquid. This was done by using a modified Mott analysis (Refs. 8 and 9). This analysis allows the calculation of an interatomic stability

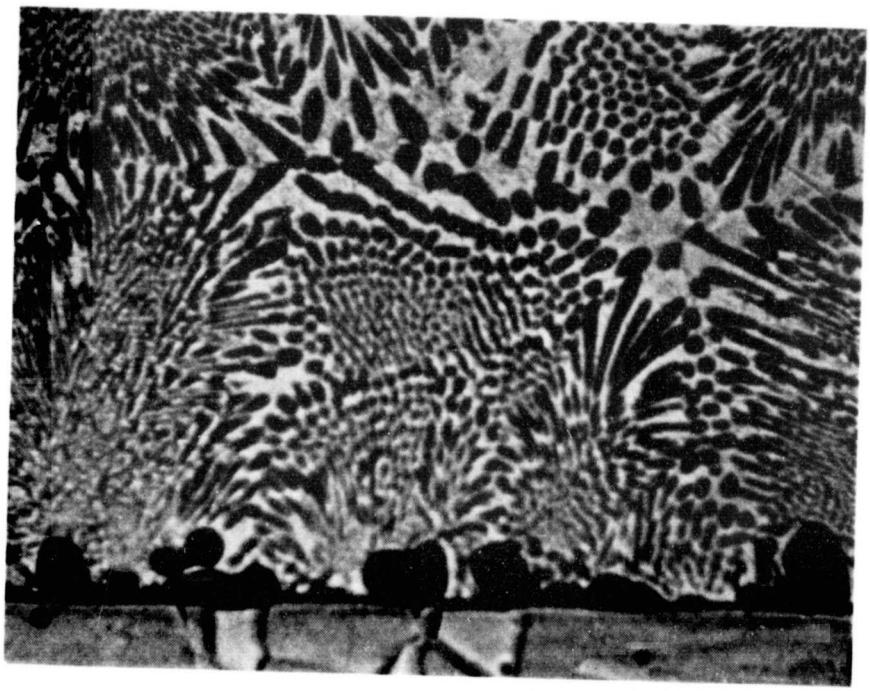

Fig. 10 Normal Brazement Eutectic Microstructure Noted in the MCN and MCS Samples (750 X)

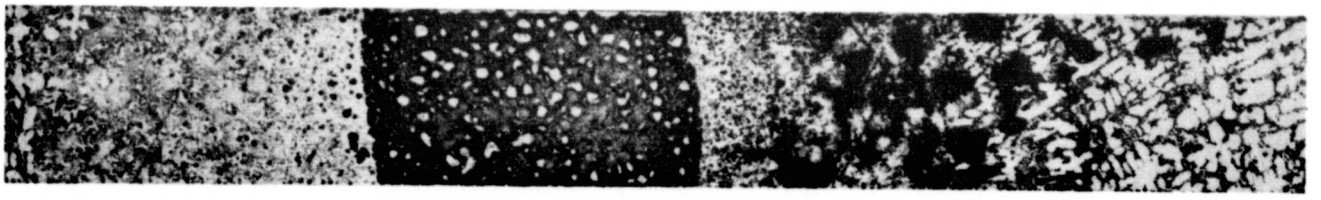

(a) Abnormal Phase Separation Noted in the SLS-3 Flight Sample (40 X)

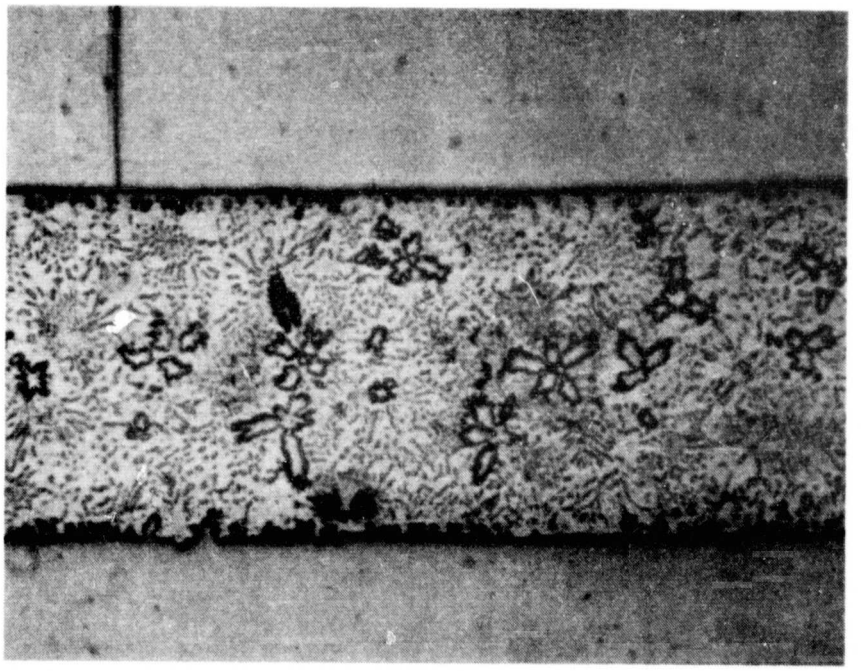

(b) Abnormal Microstructure Noted in the SLN Flight Samples (100 X)

Fig. 11 Abnormal Microstructures Noted in the M552 Flight Samples

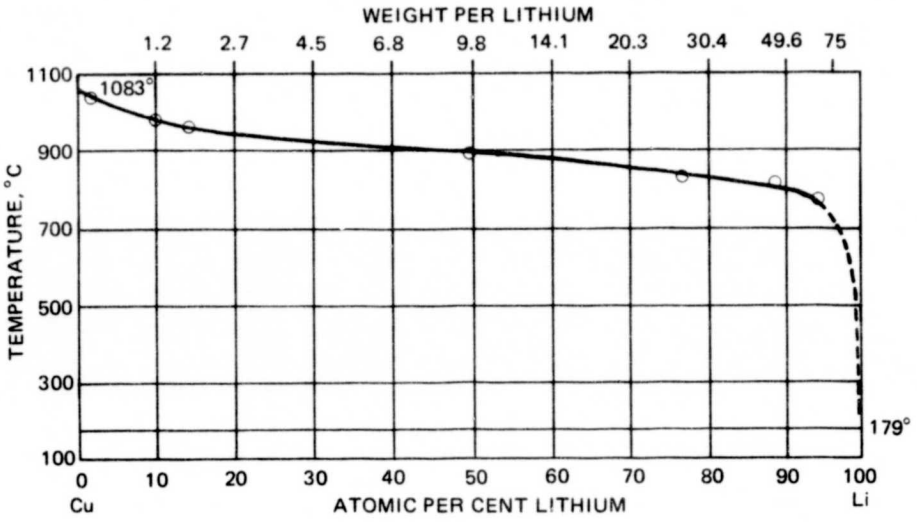

(a) Copper – Lithium

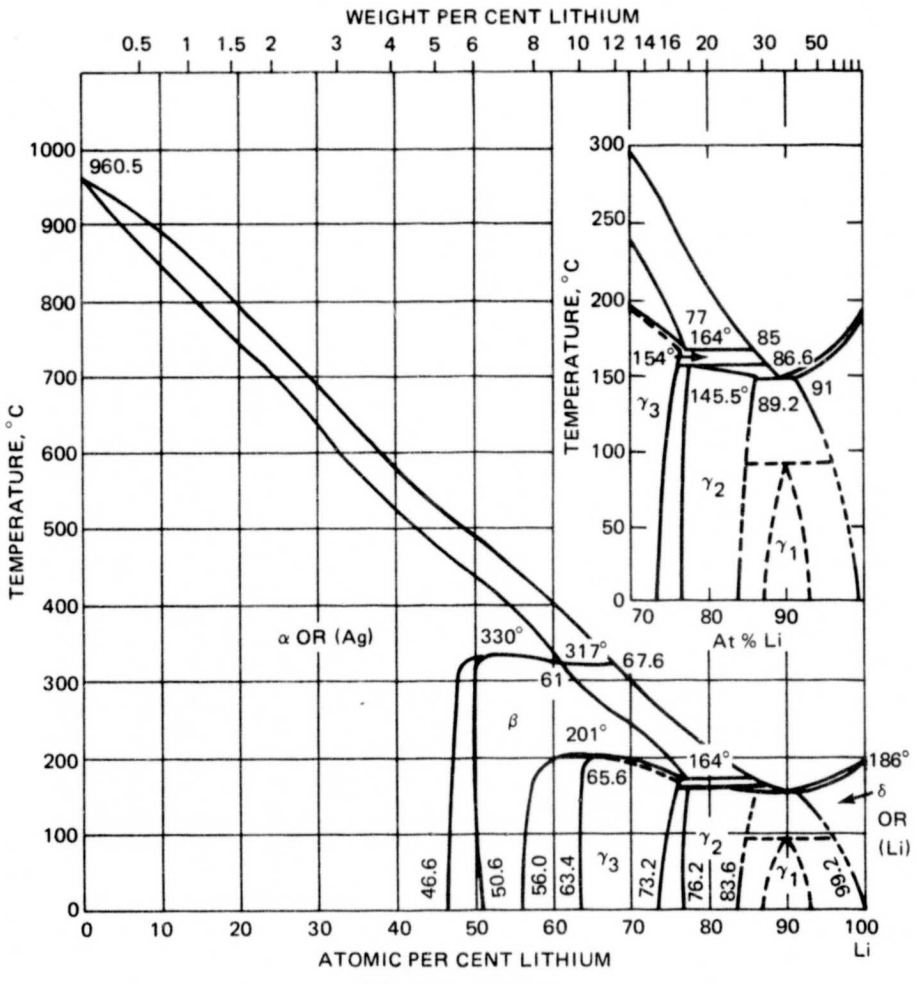

(b) Silver Lithium

Fig. 12 Copper Lithium and Silver Lithium Binary Phase Diagrams

index, referred to as a Mott number. If the calculated Mott number is plotted versus the size difference of the binary atom pairings, then a regime will be defined within which liquid/liquid immiscibility would be anticipated. As may be seen in Fig. 13, our calculations show that the Ag/Cu liquid is only marginally stable. A small perturbation in the direction of greater size difference or higher Mott Number is likely to be sufficient to induce immiscibility. Of the available base metal elements, our calculations show that the one most likely to provide this perturbation is nickel, or a combination of elements including nickel. In practice, some dissolution of base metal occurs and, thereby, causes a change in the elemental constituency of the braze metal. Nickel was available in both of the base metals under study.

If the lithium is assumed to be totally within the silver terminal solid solution phase, then we can limit our thinking to the Cu-Ag-Ni pseudo-ternary phase diagram where Ag is actually Ag + Li. This diagram (Ref. 10) is shown in Fig. 14 up to 1873K (1600°C). We tested the validity of this assumption using a nuclear microprobe technique for lithium determination (Ref. 15) that is described in Appendix A. The lithium content for ground base sample MCN2-3 is shown in Fig. 15. The mean lithium content was 2,650 wt. ppm with a standard deviation of ±200 wt. ppm. This is well within the brazement supplier's specifications. We could not locate the Li relative to the Ag and Cu, so we analyzed the sample showing phase separation. The lithium distribution of the SLS 355 flight sample is shown in Fig. 16. The lithium content of the Cu-rich portion of the sample has a mean value of 90 wt. ppm with a standard deviation of ±45 wt. ppm. The mean value of lithium content on the left side of Fig. 16, in the Ag-rich region, is 1075 wt. ppm with a standard deviation of ±160 wt. ppm. The mean value of the right side is 810 wt. ppm, with a standard deviation of ±175 wt. ppm. It is clear that the lithium is virtually all within the Ag-rich terminal solid solution phase, and that our assumption is correct.

It is clear from Fig. 14 that above 1708K (1435°C) there is liquid/liquid immiscibility in the binary Ag-Ni diagram. This has been discussed previously (Ref. 7); however, the region of liquid/liquid immiscibility projects downwards in temperature in ternary space (Ref. 11). This is

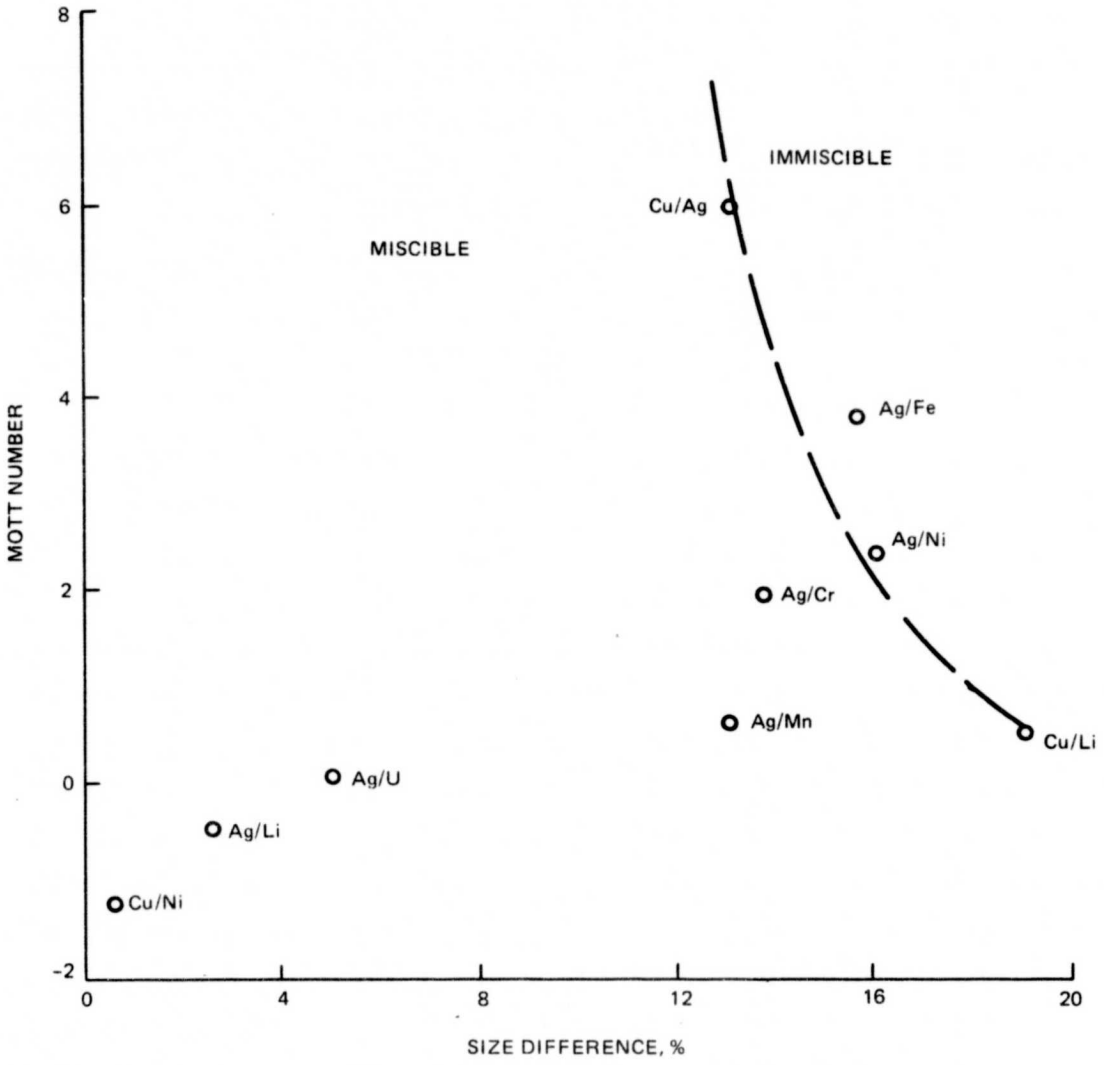

Fig. 13 Plot of Calculated Mott Number Vs Size Difference for the M552 Experiment Constituent Elements. The dashed line indicates the onset of instability

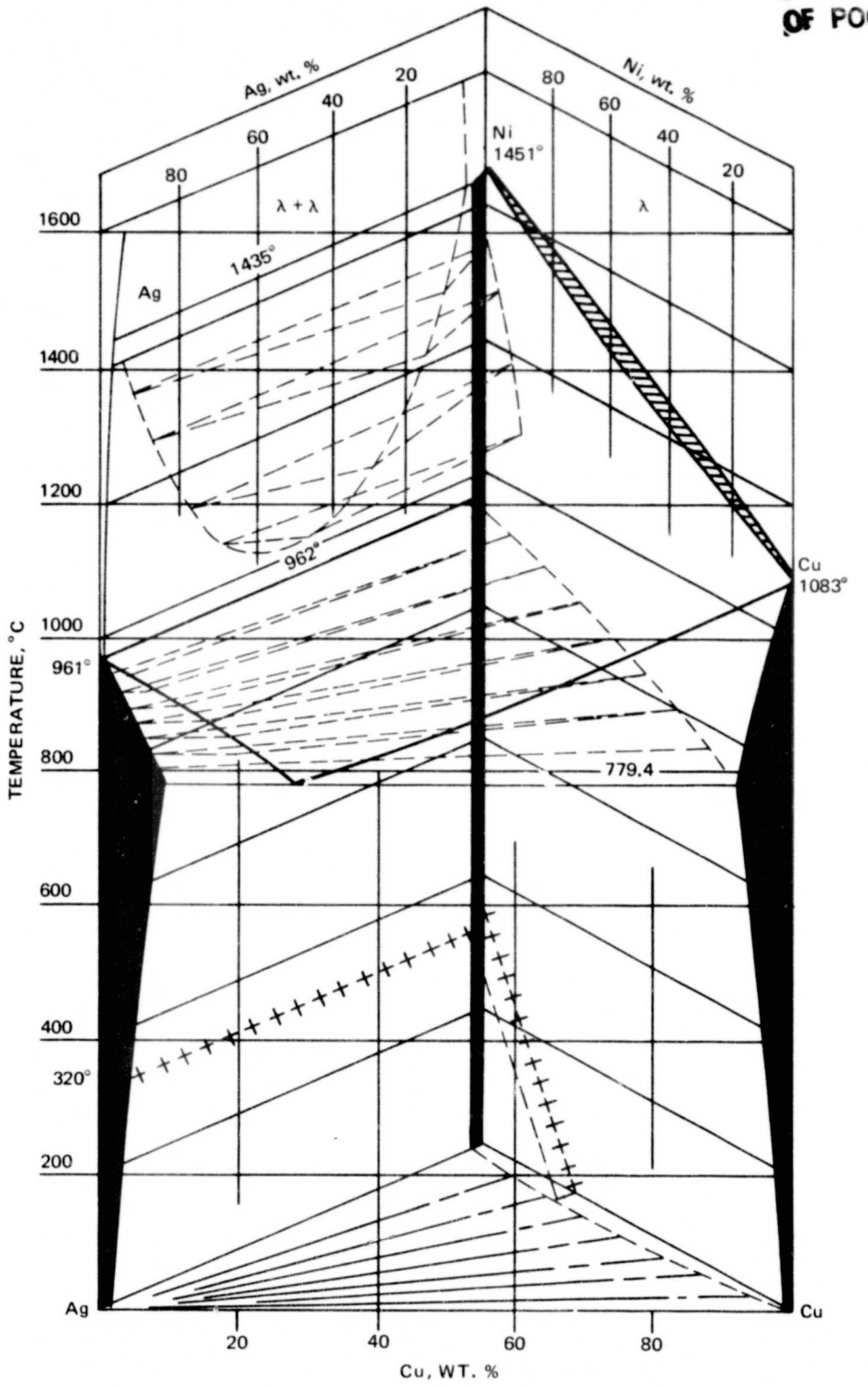

Fig. 14 Silver-Copper-Nickel Ternary Phase Diagram

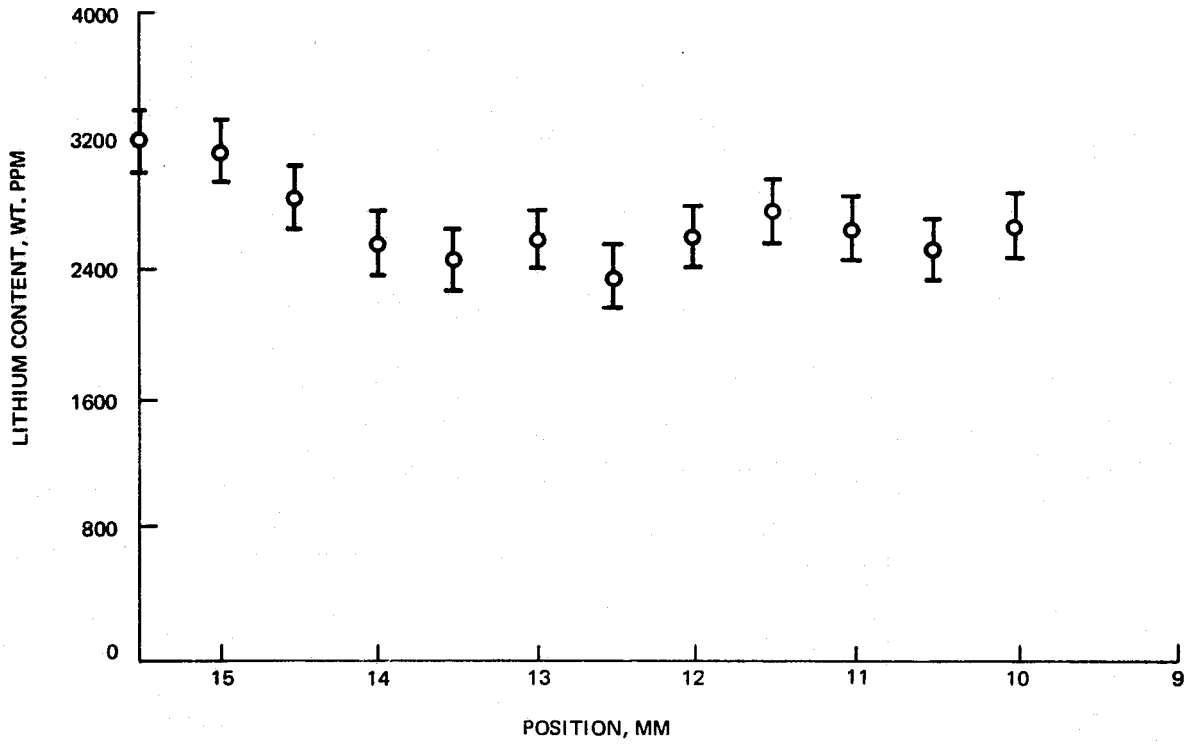

Fig. 15 Lithium Profile Within the MCN 2-3 Ground Base Sample Brazement

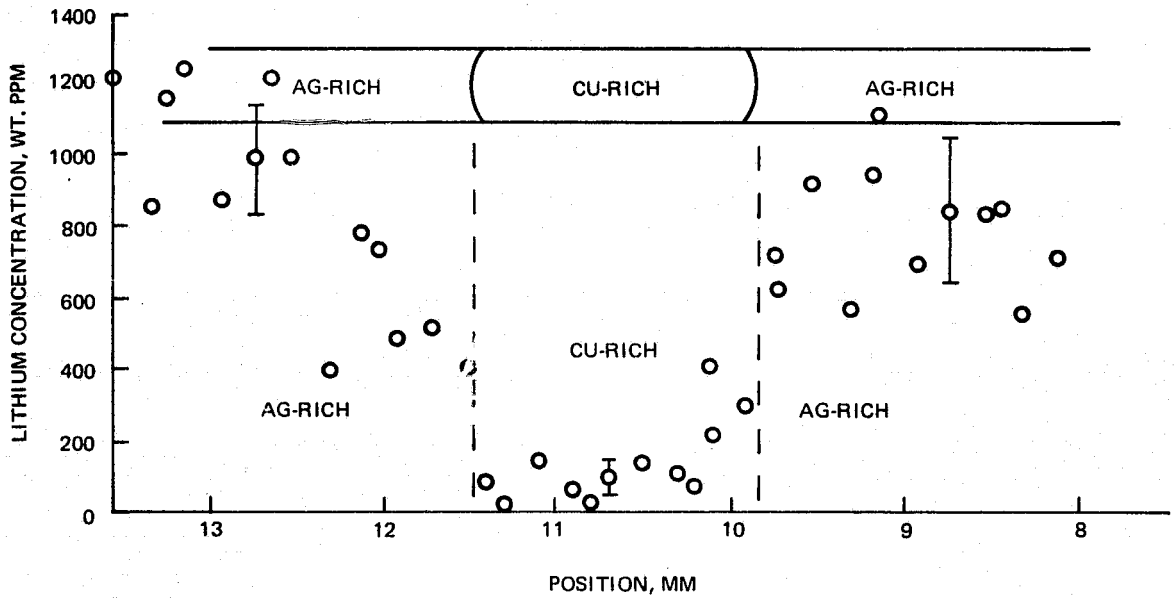

Fig. 16 Lithium Profile Within the SLS 355 Flight Sample Brazement With Superimposed Schematic of the Corresponding Location Within the Brazement

shown in Fig. 14. An isothermal ternary section taken at 1673K (1400°C) is shown in Fig. 17a (Ref. 12), and the reported ternary liquidus curves (Ref. 12) at temperatures varying from 1673K (1400°C) to 1073K (800°C) are shown in Fig. 17b. We have hypothesized that the origin of the curvature of the liquidus curves in Fig. 17b is the ternary liquid/liquid immiscibility that extends downwards in temperature to the vicinity of 1373K (1100°C). This is consistent with the data presented as Fig. 14 (Ref. 10). This is close to the maximum temperature reached in the course of the ground base experimentation (Ref. 8), and calculations have shown that the flight samples may have reached 1423K (1150°C).

The actual temperature profiles and the time/temperature history could not be measured during the flight experimentation. Profiles were measured during the ground base simulations (Ref. 13). These data have been replotted and are presented as Fig. 18. It should be noted from Fig. 18 that the time to peak temperature was approximately 60 seconds and the peak temperature reached was about 1328K (1055°C). The thermal profile during cooling and solidification approximated that of an isothermal lowering process. No strong non-isothermal component was expected. The brazements were in a molten state for about 200 seconds. It therefore appears that:

- The Cu-Ag liquid is only marginally stable
- Nickel is a candidate element to induce liquid/liquid immiscibility
- Nickel was available in both base metals studied
- Cu-Ag-Ni ternary liquid/liquid immiscibility can extend downwards in temperature to 1373K (1100°C)
- The peak experimental temperature measured on the ground was 1328K (1055°C) and could have realistically reached 1373K (1150°C) in the flight samples

If ternary liquid/liquid immiscibility was encountered above 1100°C, it should be possible to explain all of the microstructures previously recorded as abnormal (Refs. 6 and 7) on the basis of ternary Cu-Ag-Ni solidification considerations. The critical Cu-Ag-Ni isothermal sections are presented as Figs. 19a and 19b.

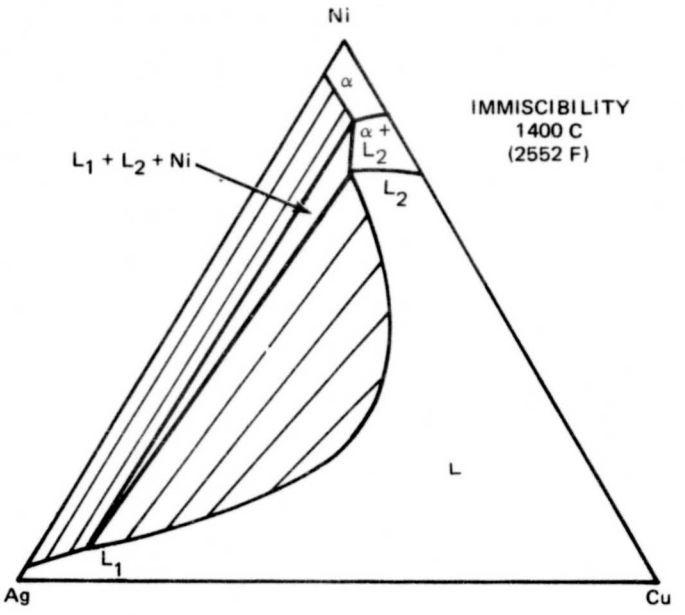

(a) Isothermal Section at 1673K (1400°C)

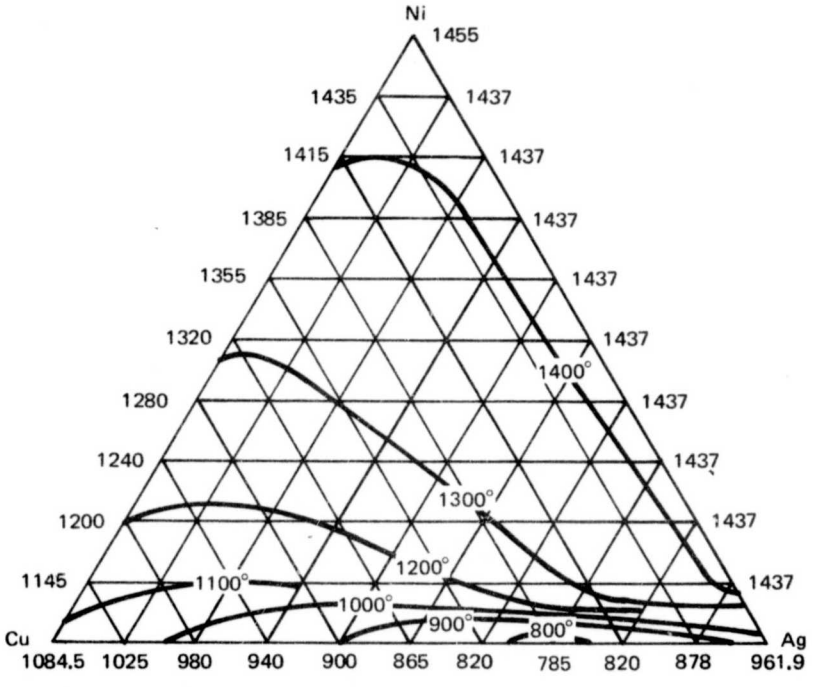

(b) Ternary Ag-Cu-Ni Liquidus Curves

Fig. 17 Ag-Cu-Ni Phase Relationships

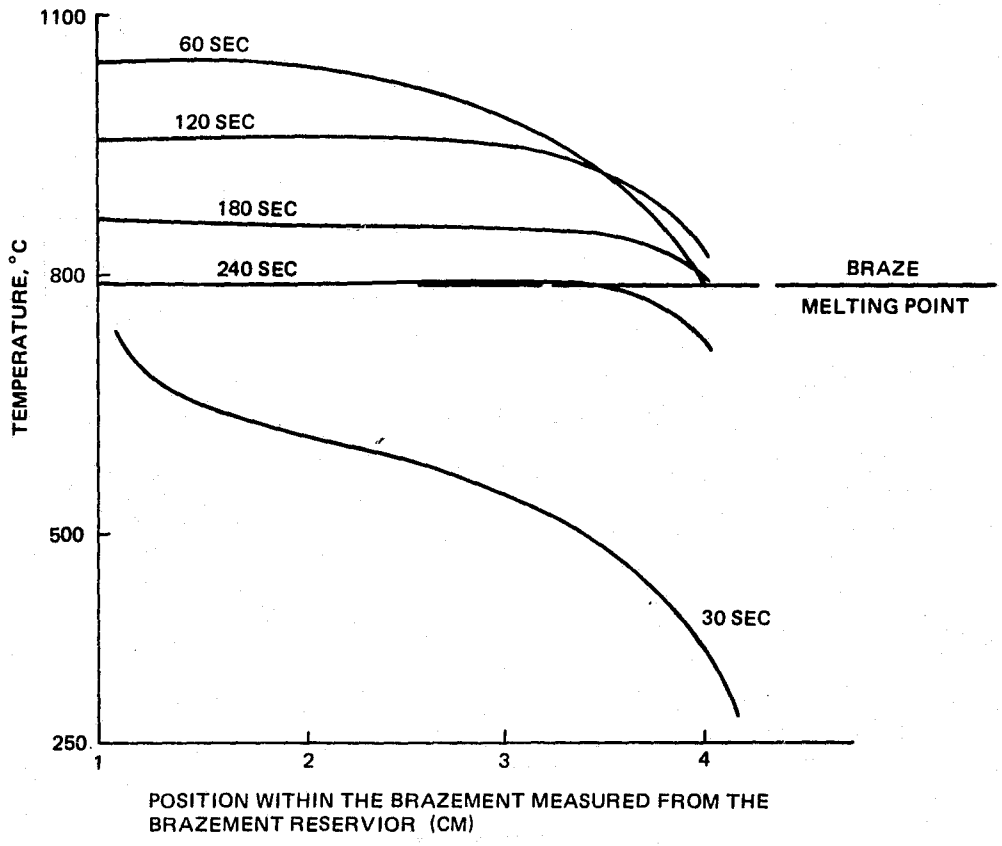

Fig. 18 Isochronal Thermal Profiles within the Brazement during the Ground Base M552 Experiment

If the brazement temperature never exceeded 1373K (1100°C), then the ternary phase relations can be explained using Fig. 19a. This seems to be the case for the ground base experiments. The liquid brazement eroded the base metal and absorbed nickel until a steady state was achieved or the processing time at temperature expired. The local alloy composition with maximum nickel content, determined by EDAX, was 5% Ni - 28% Cu - 67% Ag. Solidification of this system took place by primary growth of Cu-Ni dendrites (65% Ni - 30% Cu - 5% Ag) followed by secondary growth of Cu-Ni and Ag-Cu dendrites; finally the tertiary eutectic reaction completed solidification.

When the brazement temperature exceeded 1373K (1100°C), the ternary phase relations changed appreciably. This is shown in Fig. 17b. As in the previous case, nickel was absorbed within the liquid brazement. The resulting alloy compositions are indicated by a dotted line within Fig. 19b. As nickel is absorbed, the first two-phase region that is encountered is the L_1 and L_2 miscibility gap. Therefore, liquid/liquid phase separation results at the nickel interface. The copper-rich liquid, L_1, remains in contact with the nickel base metal because it has a substantially lower interfacial free energy with the nickel or stainless steel base metal (275 ergs/cm^2) than does the silver-rich liquid (1200 ergs/cm^2). This results in a copper-rich 'coating', which, if solidified, gives an uneven appearance to the interface because it solidifies dendritically. This uneven interface has been previously observed by Heine (Ref. 7) in samples that were not assumed to have experienced liquid/liquid separation. As this reaction goes further to completion, the immiscible phases assume a lower energy configuration, and the phase distribution consists of a copper-rich layer adjacent to the base metal with any excess copper-rich liquid forming a single sphere within the silver-rich liquid. The SLS-3 sample shown in Fig. 11a exhibits this morphology, except that the aspect ratio is such that the sphere has contacted the thin layers at the base metal interfaces, forming a complex geometry. The solidification sequence following the phase separation is shown schematically in Fig. 20.

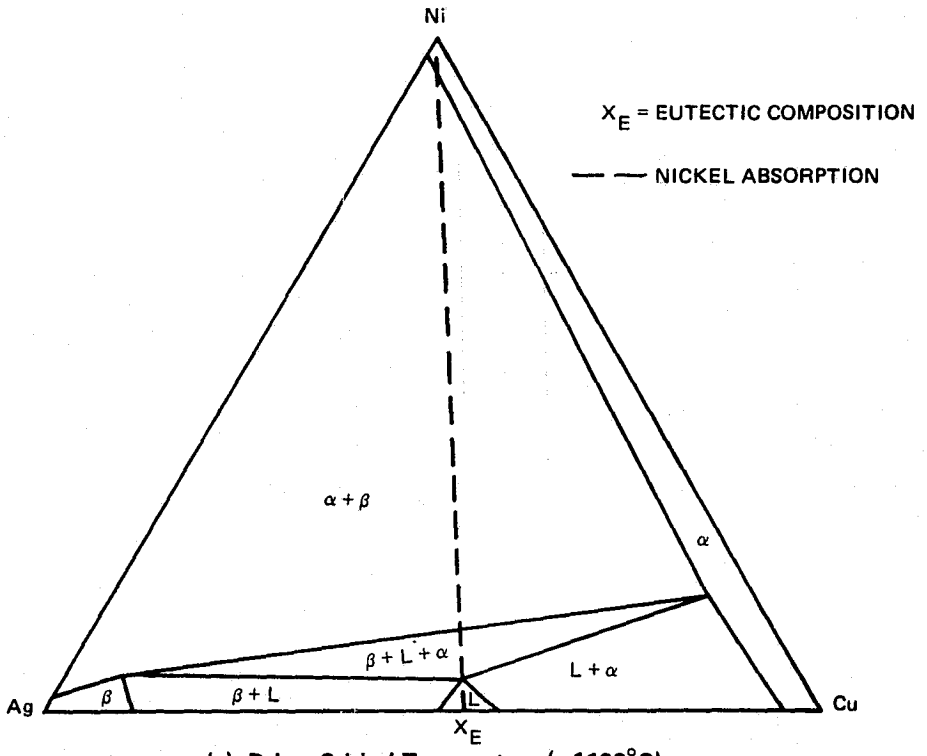

(a) Below Critical Temperature (~1100°C)

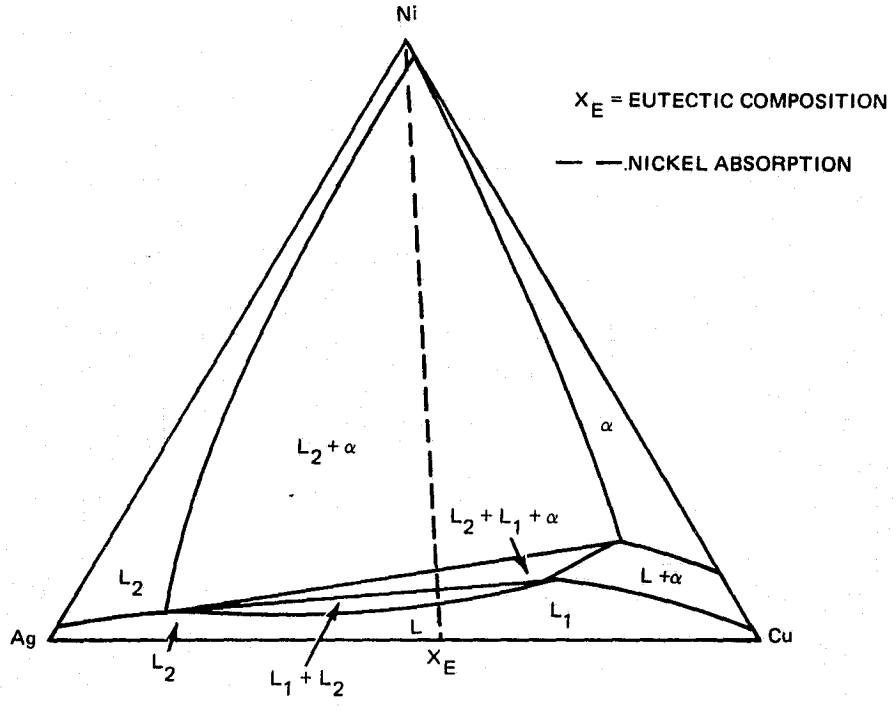

(b) Above Critical Temperature (~1100°C)

Fig. 19 Silver-Copper-Nickel Phase Relationships at Temperatures below and above 1373°K

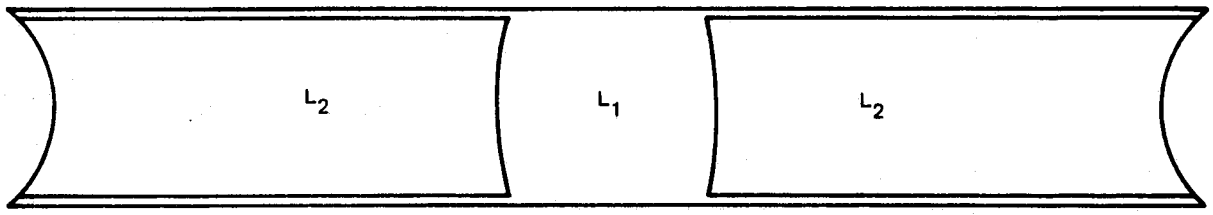

(a) T > 1356K (1083°C)

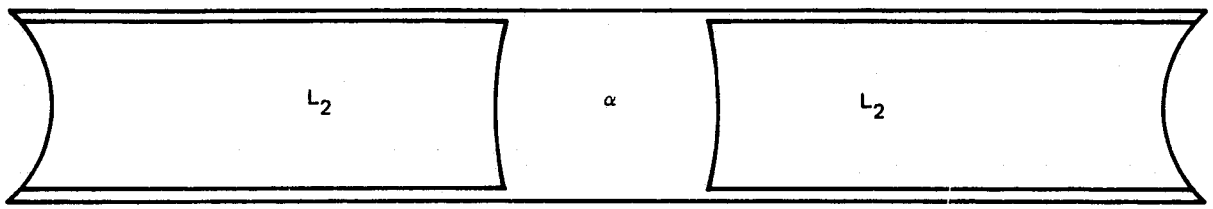

(b) 1356K (1083°C) > T > 1233K (960°C)

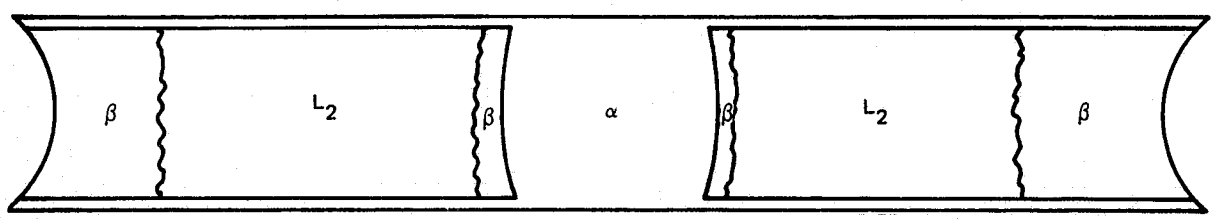

(c) 1233K (960°C) > T > 1052K (779°C)

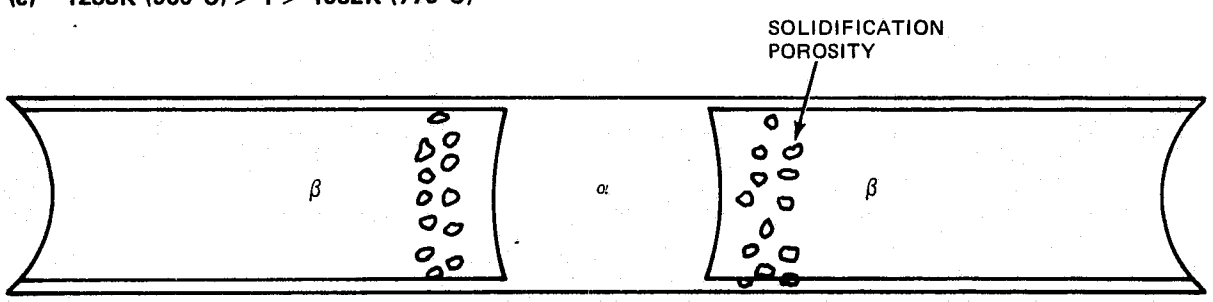

(d) 1052K (779°C) > T

Fig. 20 Proposed Solidification Sequence within the SLS 355 Flight Sample after Superheating above 1100°C

As the nickel content continues to increase, the region of liquid/liquid immiscibility is traversed and the copper-rich liquid decomposes to solid Ni-Cu plus silver-rich liquid. This was estimated to occur between 6 and 8% Ni. This would give the copper-rich liquid a multiphase appearance. This has also been observed by Heine (Ref. 7) and has been described as 'porous' in appearance.

When nickel absorption totally consumes the copper-rich liquid only Ag-rich liquid, L_2, and solid Ni-Cu can coexist. The solidification structure of this liquid/solid array is then a fine dispersion of particles of Ni-Cu within a solidified silver-rich liquid. This microstructure is shown as Fig. 11b and occurred when the Ni in solution exceeded 8%. This reaction would eliminate the interfacial layer that solidifies as coarse Cu-rich dendrites, thus giving the interface a smooth appearance. The Ni-Cu particles and solidified Ag-rich liquids have been observed by Heine (Ref. 7) within the SLN flight samples and have been termed 'anomolous'. He also mapped the gap widths, corresponding microstructures, and interface flatness and reported an exact correlation with what we have presented on the basis of phase equilibria. We attribute the higher nickel contents to higher peak temperatures and longer times at temperature due to the near absence of convective heat transfer in the flight samples.

Equilibrium Liquid/Liquid Configurations

The lowest energy configuration of one fluid arrayed within another is that of a single sphere (Ref. 16). All other configurations increase the interfacial area, and, since the interfacial energies are typically high, the total energy is significantly increased. It is clear, then, that a fine dispersion of fluid particles within another fluid is energetically unfavorable. This is the driving force behind the agglomeration process. The greater the interfacial energy relative to the volume free energy, the greater the driving force for agglomeration. Whether agglomeration takes place, however, is a question of kinetics. Experiments with liquid metals indicate that controlling these kinetics is an ambitious project, even in low-g.

In the one-g terrestrial environment, it is difficult to process immiscible liquids because the heavier (lighter) dispersed liquid settles (rises) resulting in a stratified structure with the heavier (lighter) fluid in a bottom-most (top-most) position. It was thought that in the near absence of gravity the forces principally responsible for the sedimentation and agglomeration processes would be nearly eliminated and that uniform, fine-scale dispersions of immiscible liquids would result. Achieving this has proven to be more difficult than anticipated, and although more symmetrical dispersions have been achieved, they have been on a macroscopic, scale, as described herein for the M557B and M552 liquid/liquid immiscible samples. In this light, it might be best to return to fundamentals in order to assess which processes are deleteriously impacting the results and are negating the gravitational advantage.

Markworth, et al. (Ref. 17) have suggested that the final solidified structure of an immiscible sample will depend on the following kinetic processes:

- Nucleation of second phase liquid droplets within the host phase
- Growth of the liquid droplets to achieve the equilibrium volume fraction of dispersed phase
- Coalescence of the droplets (specific mechanisms will be considered subsequently)

The nucleation and growth mechanisms are not thought to be gravitationally related and occur in an extremely rapid time frame that makes them unattractive as control parameters. As a result, we will focus on the coalescence of droplets.

Coalescence - The coalescence of droplets may occur by any of the following mechanisms, after Markworth, et al. (Ref. 17):

- Direct impingement of growing droplets
- Impingement resulting from Brownian-motion
- Impingement resulting from Stokes flow
- Impingement resulting from Thermo/solutal convective flow

- Impingement resulting from Marangoni flow
- Ostwald ripening

Papazian (Ref. 18) has added the following mechanisms to the above:

- Impingement due to capillary effects
- Impingement due to flow originating from the volumetric change of solidification

The author has added the following mechanism:

- Impingement due to fluid flow originating from the rapid displacement of fluid during the coalescence of droplets

The Stokes flow and thermo/solutal convective flow mechanisms are gravitationally dependent and are thereby minimized by orbital processing. It is our conclusion, however, that the processing of high volume fraction liquid/liquid immiscible alloys (> 20 vol. % dispersant) places the particles in very close proximity to one another (typically less than one particle diameter). The translational distances are therefore minimal for coalescence until the particles are macroscopic in dimensions. It is our conclusion, as well, that some of the coalescence mechanisms specified have the potential for rapid displacement of fluid even in the low-g environment, and that these mechanisms are sufficient to cause the dispersion to approach the equilibrium liquid/liquid configuration in anything other than extremely short processing times, highly viscous host liquids, or very low volume fraction systems.

It should also be pointed out that the equilibrium fluid array will depend on the interfacial energies of the fluids in contact with each other, the container, and residual atmosphere; container total volumetric fill factors; volume fraction of dispersed phase; and length-to-diameter ratio of the container. These agglomeration mechanisms and fluid/container equilibrium arrays will be quantitatively assessed in a future work.

LIQUID/SOLID PHASE SEPARATION

Experiments of this type have behaved as expected, and processing of solid/liquid dispersions has resulted in uniformly dispersed particulate

arrays. Reger (Ref. 4 and 5), Takahashi (Ref. 19), and Larson (Ref. 20) have all observed greatly improved chemical homogeneity within the orbitally processed materials of this type. The agglomeration of solid particles is not as likely as in the case of fluid particles. The resultant arrays are thus uniformly dispersed and on a fine scale. Takahashi (Ref. 19) has reported enhanced mechanical strength in the orbitally processed materials, and Heye and Klemm (Ref. 21) have reported beneficial superconductive effects, presumably due to flux pinning. Both effects are reported to be due to more uniform particulate dispersions. It is reasonable to conclude that solidification processing dispersions of immiscible solid particulate matter will be benefitted by orbital processing. In addition, processing alloys with substantial thermal or compositional differences between their liquidus and solidus lines will be benefitted in the same manner during nonplanar solidification.

M557A Isothermal Solidification of Hypereutectic Au-Ge

The M557A Skylab Experiment conducted by Reger (Ref. 1 and 2) solidified a hypereutectic Au-23.15 wt. % Ge alloy in the absence of a thermal gradient. There is a 250°K temperature difference between the liquidus temperature and the isothermal eutectic reaction for this alloy. There is also an appreciable density difference between the proeutectic Ge crystallites and the residual Au-rich liquid. Additionally, buoyancy segregation occurs on a macroscopic scale.

The M557A Skylab Experiment demonstrated that buoyancy driven solid/liquid segregation is virtually eliminated by orbital processing. Microstructural and resistivity data showed that a homogeneous product had been fabricated in space. Reger (Ref. 1 and 2) reported, however, unknown diffraction lines for the flight samples. This study was conducted to determine the origin of these anomalous diffraction spectra. The anomolous diffraction lines are listed in Table 3, column 1. Our calculated diffraction spectra for elemental Au and Ge are shown in columns 2 and 3, respectively. Clearly, those lines reported as anomolous are due to higher order reflections of the elemental species. This conclusion is supported by an independent study conducted by Horton (Ref. 22). Our work, shown in column 4, showed no anomolous diffraction lines and, hence, no metastable phases. The Au, face-centered cubic lattice parameter was

TABLE 3 CALCULATED AND EMPIRICAL DIFFRACTION SPECTRA FOR THE M557A SKYLAB SAMPLES

Unknown Diffraction Spectra Reported by Reger	Calculated Diffraction Spectra		Experimental Observations
	Ge	Au	
	3.267		
		2.355	2.350
		2.039	2.038
1.992	2.000		
	1.706		1.703
		1.442	1.442
	1.415		
1.293	1.298		1.296
		1.230	1.230
		1.177	1.176*[2]
	1.155		
	1.089		
1.021		1.020	
	1.000		
	0.956		
	0.943		
		0.936	
0.910		0.912	
0.893	0.895		
	0.863		
0.833		0.832	
0.831*[1]			
	0.817		

*[1] This peak may be due to $K_{\alpha 1}$, $K_{\alpha 2}$ resolution at these high angles. We did not have the films available and cannot comment further.

*[2] Our diffractometer scans were terminated at d = 1.150.

found to be 4.075 ±.002 Å. The Ge, diamond cubic lattice parameter was found to be 5.648 ± 0.002 Å.

Although Rhines (Ref. 11) has suggested that variation of the gravitational constant will result in an extra variable to be considered in the phase rule, a thermodynamic calculation by Oriani has shown this to be incorrect. In short, one would not expect fundamental differences in phase relationships due strictly to the variation of the gravitational level. Oriani's proof is included as Appendix B. This is consistent with our conclusion that no unidentified phase exists within the M557A or M557B experiment samples.

M557C Directional Solidification of a Ternary Pb-Sn-In Eutectic

The M557C experiment involved the directional solidification of a 70.2 - 14.8 - 15.0 wt. % Pb-Sn-In alloy. Pb is the primary phase to solidify, and the secondary phases are Sn, In_3Pb and γ Sn-In. We have estimated that for directional plane front solidification of this alloy a G/R ratio of the order of $1 \times 10^6 \frac{K\ sec}{cm^2}$ is required. The average G/R reported for this experiment was about $1 \times 10^5 \frac{K\ sec}{cm^2}$. This was insufficient to stabilize a plane front interface. Our microstructural evidence indicates that plane front solidification did not occur within the bulk of the sample. This is shown in Fig. 21.

Reger (Refs. 4 and 5) reported anomolous x-ray diffraction lines for these samples, as well. These are included as column 1 in Table 4. Once again, these lines are attributable to constituent equilibrium phases and are not anomolous in nature. The calculated diffraction spectra for the four equilibrium phases are included in Table 4 as columns 2-5, and our experimentally determined spectra are shown in column 6. It is clear that all of the diffraction lines are explicable on the basis of the equilibrium phases.

We found effects of the absence of hydrostatic pressure within these samples, as shown in Fig. 22. In the near-absence of the gravitationally dependent hydrostatic pressure head, the non-wetting liquid column will

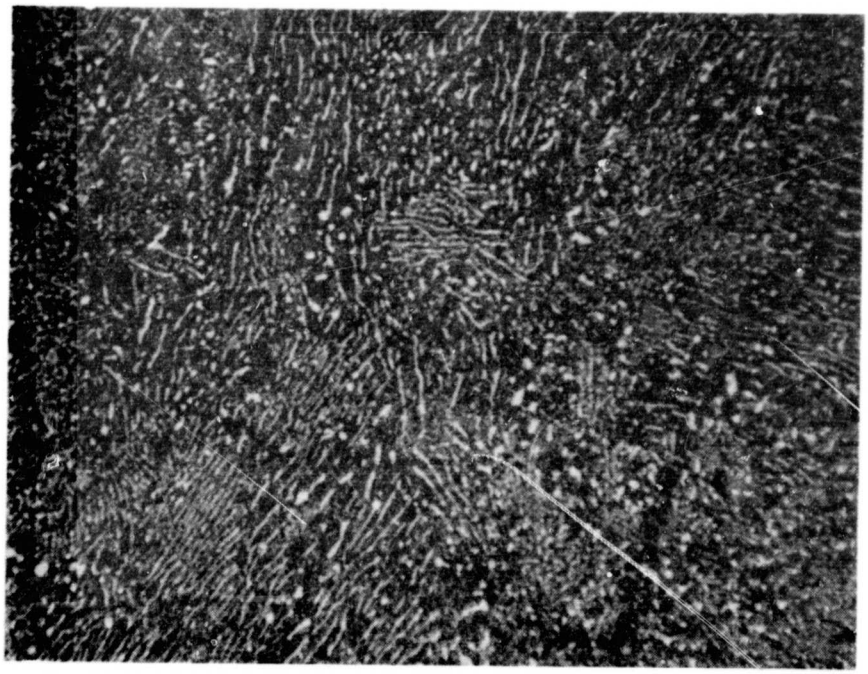

Fig. 21 Longitudinal Microphotograph of M557C Sample 3C-1 Showing the Absence of Plane Front Directional Solidification. (Growth is in the vertical direction) (250X)

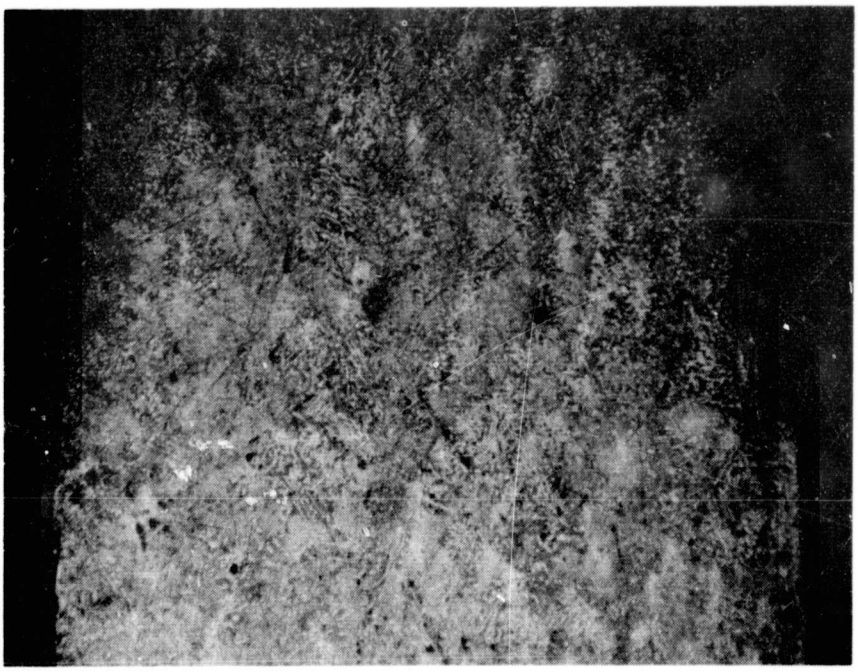

Fig. 22 Melt-Back Interface of an M557C Flight Sample Showing Entrapped Bubbles within the Remelt Portion of the Sample and a Reduced Cross-Sectional Area Resulting from the Near-Absence of the Hydrostatic Pressure Head (10 x)

TABLE 4 CALCULATED AND EXPERIMENTAL DIFFRACTION SPECTRA FOR THE M557C SKYLAB SAMPLES

Unknown Diffraction Lines Reported by Reger	Calculated Diffraction Lines					Experimental Results
	Pb	Sn	In_3Pb	Sn-In		
		5.831				
			4.880			
			4.540			
		4.123				
			3.451			
			3.323			
		3.182				3.146
3.048				2.998		3.015
		2.916				
2.840	2.858					2.942
		2.793		2.785		2.798
			2.747			
		2.519				
	2.475					2.462
			2.440			
			2.269			
		2.150				
				2.041		2.042
	1.750		1.725			1.736
	1.492			1.499		1.480
	1.429					1.421
		1.414		1.417		1.417

assume a cross-section determined by surface tension forces rather than conforming to the shape of the ampoule as in the terrestrial environment. This is a rather graphic illustration of the increased significance of surface tension forces in the low gravity environment. In addition to a reduced cross-section, there was a substantially increased bubble content within the flight samples. This is due to the virtual elimination of buoyancy forces that would have eliminated these bubbles in the terrestrial environment.

RESULTS AND CONCLUSIONS

The microstructures and diffraction spectra of low-gravity processed samples that were previously reported to be anomalous or representative of metastable phases have been explained on the basis of equilibrium phase relations. This is consistent with an included thermodynamic derivation that predicts that metastable phases are not to be anticipated solely on the basis of the reduction of the gravitational level.

The Skylab M557B Pb-Zn-Sb immiscible samples processed in the low-gravity environment exhibited a more uniform distribution of phases than those processed on the ground. The more uniform distribution of equilibrium phases in the flight samples resulted in more diffraction lines being detected in the flight samples than in the segregated ground base samples. These additional lines had previously been reported to be anomalous. We found the additional lines to be due to equilibrium Zn_3Sb_2 and Sb. The crystal structure of the Zn_3Sb_2 phase, previously unknown, has been identified as complex hexagonal with a_o = 8.14 Å and C = 17.68 Å. The solidified immiscible phases within the flight samples were macroscopic in dimensions; that is, considerably coarser than anticipated.

The microstructures of the Skylab M552 Ag-Cu-Li low gravity processed brazements, previously reported to be anomalous, have been explained on the basis of pseudo-ternary phase equilibria.

The previously reported anomalous x-ray diffraction spectra for the low gravity processed Skylab M557A Au-Ge and M557C Pb-Sn-In samples have been shown to be due to reflections from the constituent phases.

The reduction of gravity in the orbital environment has resulted in the reduction of the hydrostatic pressure head and buoyancy forces in the M557C flight samples. The reduction in internal pressure within these samples permitted the surface tension forces to pull the nonwetting liquid column away from the crucible walls. The reduction in buoyancy forces has resulted in an increased number of bubbles entrapped within the Pb-Sn-In solid.

ACKNOWLEDGEMENTS

This work was conducted with partial support from NASA contract NAS 8-28728, for which the author is grateful. The author would also like to thank Drs. Papazian, Geschwind, and Adler for helpful suggestions on the conduct of this investigation and constructive criticism of the final report. The author is particularly grateful to Dr. Robert Schulte of the Grumman Research Department's Nuclear and Astrophysics Laboratory for conducting the nuclear microprobe analysis for lithium. The author would also like to thank Dr. R.A. Oriani of the United States Steel Research Laboratory for permission to include his unpublished work in this report.

REFERENCES

1. J.L. Reger, Proceedings of the Third Space Processing Symposium; Skylab Results: Vol. 1, N.T.I.S. Report No. M-74-5, pp.133-158, June 1974.

2. J.L. Reger, Final Report on NASA Contract NAS 8-28309, TRW Systems Group Report 22457-6016-RU-00, April 1975.

3. J.L. Reger, Interim Report on NASA Contract NAS 8-28267, TRW Systems Group Report 14725-6010-RU-00, May 1973.

4. J.L. Reger and I.C. Yates, Jr., AIAA Paper No. 74-207.

5. D.T. Klodt, Ph.D. Thesis, 1965, University Microfilms, Ann Arbor, Michigan.

6. J.R. Williams, Proceedings of the Third Space Processing Symposium; Skylab Results: Vol. 1, N.T.I.S. Report No. M-74-5, pp. 33-84, June 1974.

7. R.W. Heine, T.A. Siewart, C.M. Adams, 10 Month Report on NASA Contract No. NAS 8=28733.

8. C. Dasarathy, Trans. AIME, Vol. 245, pp. 2015-19, 1969.

9. B.E. Sundquist, Trans. AIME, Vol. 236, pp. 1111-1122, 1966.

10. W. Guertler, et. al, N.T.I.S. Document TT69 55069, p. 229, 1969.

11. F.N. Rhines, Phase Diagrams in Metallurgy, McGraw-Hill Book Company, Inc., 1956.

12. Metals Handbook, Volume 8, ASM Publication, p. 380, 1973.

13. T. Muraki and K. Masubuchi, Report on Contract NAS 8-28732, M.I.T., December 1973.

14. Metals Handbook, 1948 Edition, ASM Publication,1948.

15. G. Padawer, U.S. Patent No. 3,710,113, Lithium Nuclear Microprobe, January 9, 1973.

16. J.W. Cahn, Trans. Met. Soc., AIME, Vol. 242, p. 166, 1968.

17. A.J. Markworth, S.H. Gelles, J.J. Duga and W. Oldfield, Proceedings of Third Space Processing Symposium; Skylab Results: Vol. 2, N.T.I.S. Report No. M-74-5, p. 1003, June 1974.

PAGE 42 INTENTIONALLY BLANK

18. J.M. Papazian, private communication (In Publication).

19. S. Takahashi, Proceedings of the Third Space Processing Symposium; Skylab Results: Vol. 1, N.T.I.S. Report No. M-74-5, June 1974.

20. D.J. Larson, Jr., Final Report on NASA Contract NAS 8-30577, Grumman Research Department Report RE-532, December 1976.

21. W. Heye and M. Klemm, NASA Technical Memorandum NASA TMX-3458, SPAR-I Final Report, December 1976.

22. R.M. Horton, Scripta Metallurgica, Vol. 9, pp. 547-550, 1975.

APPENDIX A

NUCLEAR MICROPROBE TECHNIQUE FOR LITHIUM DETERMINATION

The nuclear microprobe for lithium is a nondestructive technique for the determination of lithium content within the near surface region of materials. The method employs the $^{7}Li(p,\gamma)^{8}Be$ reaction in which the incoming proton beam interacts with the lithium of the sample and emits the 14 and 17 MeV characteristic gamma rays. The gamma rays are detected by a 12.7 cm x 12.5 cm sodium iodide detector and their number is proportional to the lithium concentration of the sample. To obtain the lithium concentration, the yield of the characteristic gamma rays from the sample is compared to the yield from a reference standard whose lithium content is known. In this case, a lithium flouride crystal was used. In a resonant reaction of this type, the probing depth within the sample is dependent on the incident beam energy and the stopping power of the material under study. At the proton beam energy of 486 keV, the probing region lies at a depth of 0.3 μm below the surface of the braze material.

Samples were mounted onto a target holder driven by a micrometer screw mechanism that allows the sample to be scanned through the beam with a 0.01 mm precision in positioning. The beam spot size at the sample is 0.33 mm in diameter, so that spatial resolution of the scanning profiles is 0.33 mm. For the experimental configuration used throughout these measurements, the lower level of detectability for the detection system is 50 wt. ppm of lithium in the brazing alloy.

APPENDIX B

EFFECT OF GRAVITATIONAL POTENTIAL UPON PHASE EQUILIBRIA AND CHEMICAL REACTIONS

R.A. Oriani

Because one must do work to raise a mass m from a lower to a higher level of gravitational potential ϕ, a term $m\phi$ must be added to the usual expression for the free energy of the system (see Guggenhein, "Thermodynamics," Interscience Publishers, New York, 1949). The Gibbs free energy G may be written in differential form as

$$dG = VdP - SdT + \mu_1\, dn_1 + \mu_2\, dn_2 + \ldots + \phi\, M_1\, dn_1 + \phi\, M_2\, dn_2 + \ldots \quad (1)$$

in which V, P, S, and T are the volume, pressure, entropy and temperature of the phase in question. μ_i is the chemical potential of component i at any one, arbitrarily chosen intensity of gravitational potential ϕ (dimensions of energy per unit mass); the M_i and n_i are the molar mass and the number of moles, respectively, of component i.

Consider now a transfer of component 1 from one co-existing phase to another in mutual equilibrium, said transfer occurring at constant temperature and pressure. Hence,

$$dG^{\alpha} = (\mu_1^{\alpha} + \phi\, M_1)\, dn_1^{\alpha} \quad ; \quad dG^{\beta} = (\mu_1^{\beta} + \phi\, M_1)\, dn_1^{\beta} \quad (2)$$

where α and β designate the phases between which the transfer occurs in an environment at gravitational potential ϕ. Since the phases are in mutual equilibrium,

$$dG = Dg^{\alpha} + dG^{\beta} = 0 \quad ;$$

since what enters α comes from β,

$$dn_1^{\alpha} = - dn_1^{\beta}$$

Hence, $dG - 0 = (\mu_1^{\alpha} = \mu_1^{\beta})\, dn_1^{\alpha} + \phi\, (M_1 - M_1)\, dn_1^{\alpha}$

from which

$$\mu_1^{\alpha} = \mu_1^{\beta}$$

Thus, the condition for chemical equilibrium of a component in two phases is independent of ϕ, the magntiude of the gravitational potential.

That chemical equilibria are unaffected by the magnitude of gravity is an obvious consequence of the fact that the weight of a unit of mass (at one value of ϕ) does not change as a consequence of a change in the manner of chemical combination or of phase. Put in another way, the gravitational field is independent of phase. This is in marked contrast to the case of the electric field or the magnetic field, the intensities of which can change with change of phase.

Clearly, nothing in the above contradicts the well recognized indirect effect of gravity upon phase equilibria arising from the change of pressure within a liquid due to a change of ϕ (as an example). One also has the composition variation within a column of multi-component liquid due to the pressure variation caused by the weight of the liquid. Such phenomena are best regarded as effects of changes of the ambient pressure. That they can be caused by gravity is important to recognize, but is completely trivial from a thermodynamic point of view.